Wind Profiler Observations of Vertical Motion and Precipitation Microphysics of a Tropical Squall Line

PETER T. MAY

Bureau of Meteorology Research Centre, Melbourne, Victoria, Australia

DEEPAK K. RAJOPADHYAYA

Department of Physics and Mathematical Physics, University of Adelaide, Adelaide, Australia

ABSTRACT

Data from a wind profiler located at Darwin, Australia, have been used to examine the vertical motions and precipitation microphysics in a well-developed squall line. Both a mature and developing convective cell are well sampled. The vertical motions within the mature cell are dominated by the effect of glaciation and a convective downdraft feeding a cold pool. The strong updrafts are accompanied by supercooled water as much as 2 km above the freezing level. The two cells are separated by a narrow region of deep descent. The developing cell has a low-level maximum in upward motion coinciding with high radar reflectivity below 3 km, suggesting warm rain processes. There is a large transition region with deep descent and a stratiform region with a classic up- and downdraft circulation. The precipitation characteristics show the aggregation of ice particles as they descend in the stratiform region. Over half of the rain is seen to evaporate between 4 and 2 km. The cooling implied by this and the heating by the growth of ice particulates above the melting level balance the mesoscale circulation in the stratiform region. The Q_1 heating profile is consistent with previous studies above 4 km but shows a net cooling below this. This may in part be due to the storm being sampled when the system was mature with extensive convective downdrafts.

1. Introduction

Wind profilers have been widely used to study the full three-dimensional wind field associated with mesoscale weather systems. In particular, they can directly measure the vertical wind component within a convective environment. For example, Ralph et al. (1993) observed consistent vertical motions and pressure perturbations associated with a ducted gravity wave. With regard to flow within convective systems, Balsley et al. (1988) examined the mean profiles of vertical motions observed over a profiler at Pohnpei during convective conditions, stratiform rain, and clear sky. Other workers have concentrated on the structure of the vertical motion field (May 1991; Chilson et al. 1993; Cifelli and Rutledge 1994) and observations of the flow around the storm (e.g., Augustine and Zipser 1987). In these measurements, scatter from precipitating particles can seriously contaminate the clear-air spectrum (Fukao et al. 1985; Larsen and Rottger 1987). However, this contamination can also be used to obtain cloud

microphysical information (Wakasugi et al. 1986; Gossard 1988; Rajopadhyaya et al. 1993, 1994). This work utilizes these techniques and for the first time will relate the precipitation characteristics observed with a wind profiler to the vertical motion field observed around a deep, well-organized squall line.

Since 1989 a 50-MHz wind profiler has been located at Darwin, northern Australia. During the 1989 season the observations focused on the vertical wind over the radar. In addition the area was covered by the National Oceanic and Atmospheric Administration (NOAA) Tropical Oceans Global Atmosphere (TOGA) and Massachusetts Institute of Technology (MIT) 5-cm Doppler radar systems for DUNDEE (Down Under Doppler and Electricity Experiment; Rutledge et al. 1992). The relative locations of the profiler, MIT radar, and Darwin are shown in Fig. 1.

Darwin is a natural laboratory for studying tropical precipitation. Storms occur frequently and with a wide range of shear and stability characteristics (Keenan and Carbone 1992). The general characteristics of storms in the area have been the subject of observational campaigns over the past several years and have been discussed in detail (Keenan and Carbone 1992; Mapes and Houze 1993). The life cycle of squall lines in the area has been discussed by Rasmussen and Rutledge (1993). Storms with both maritime and continental

_____

Corresponding author address: Dr. Peter T. May, Bureau of Meteorology Research Centre, GPO Box 1289K, Melbourne, Victoria 3001, Australia.
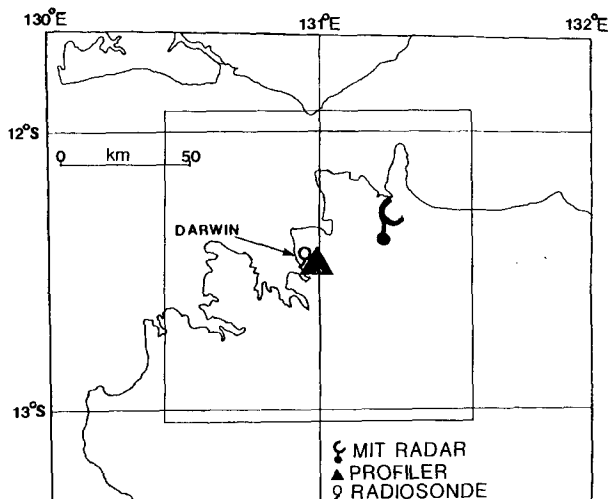E-mail: p.may@bom.gov.au

characteristics are observed during the wet season. Case studies of individual storms including dual-Doppler analyses have also been performed (Keenan and Rutledge 1992) showing details of the circulations within a squall line and its evolution. The general characteristics of a number of storms observed by the profiler have been discussed by Cifelli and Rutledge (1994).

A well-developed continental squall line was observed during the 1989–90 wet season. The convective line passed over the radar around 1800 LT 5 December 1989 [local time (central standard time), UTC + 9.5 h, will be used throughout]. The analysis includes the vertical motion and retrievals of the raindrop size distributions as well as ice crystal size distributions in the trailing stratiform region of the squall. These observations will be compared and contrasted with a similar analysis of a monsoon squall line that passed over the radar on 12 January 1990, itself the subject of detailed Doppler radar analysis by Keenan and Rutledge (1992).

2. Observational techniques

The principal instrument used is a 49.8-MHz wind profiler. The profiler observations were supported by a 5-cm Doppler weather radar to assist in the interpretation of the profiler velocity fields.

For these observations only a vertical profiler beam was used. Records were approximately 94 s long. The profiles covered heights from 1.35 to more than 20 km, although useful data often only extended to 11 km. The profiler used two modes, one with a 6 m s^{-1} Nyquist velocity and the other a "convection mode" with a 20

m s^{-1} Nyquist velocity. The convection mode was automatically selected on the basis of the mean Doppler shift and large spectral width experienced during convection or when a pronounced radar bright band was observed.

The clear-air vertical velocity was estimated by fitting a Gaussian function to the clear-air spectral peak using a least squares approach. Careful editing was performed to correct samples with biases introduced by the presence of precipitation echoes. These precipitation echoes exceeded the clear-air signal in amplitude during periods of intense rainfall and when there was an intense radar bright band in the trailing stratiform region. The uncertainty in an individual velocity estimate is a function of the radar spectral width (see May et al. 1989) and ranges from about 0.1 m s^{-1} in the stratiform and transition regions to about 0.5 m s^{-1} in the most active convection. These values are conservative and have been used to estimate the uncertainty in profiles of average vertical velocity later. The only heights where they may represent a slight underestimate of the true error are near the freezing level in the stratiform and transition regions where the bright band caused problems.

Examples of the spectra observed by the radar in convection and stratiform rain[1] are shown in Fig. 2. The convection clearly shows the clear-air echoes and the rain echoes with a reflectivity weighted fall speed of about 8 m s^{-1}. The acceleration of the vertical wind above the freezing level is a consistent and very distinct feature. In this profile, the echo from water droplets at fall speeds of about 8 m s^{-1} is seen to extend to about 7 km. This is well above the freezing level, and these spectra are used to diagnose the presence of supercooled water in the active convective region.

There was also a distinct echo from precipitating ice particles visible in the trailing stratiform region. The ice echo is frequently as strong as the clear-air echo over a significant range of heights in the trailing stratiform region. The fall speeds are naturally fairly small (0.5–2 m s^{-1}), so that great care had to be exercised to avoid biasing the clear-air estimates by the ice echoes. This is not difficult in the example shown, but there are some cases where the ice and clear-air echoes merge, although it is still possible to separate the peaks.

As may be expected, the bright band is clearly evident in the trailing stratiform region. The increase in echo power as the ice particles are coated in liquid water and the shift toward higher fall speeds are consistent features throughout the stratiform region. As will be

---

[1] The convective region is defined by reflectivity greater than 30 dBZ and vertical motions with amplitudes greater than 1 m s^{-1} (1806–1905), the transition region is defined as the weak reflectivity region behind the convection with deep descending motion (1905–1935), and the stratiform region is defined here as the region with a distinct mesoscale up- and downdraft couplet (1935–2050).

"CONVECTION"
Time = 18:53

CLEAR AIR ——
RAIN — — ·

"STRATIFORM"
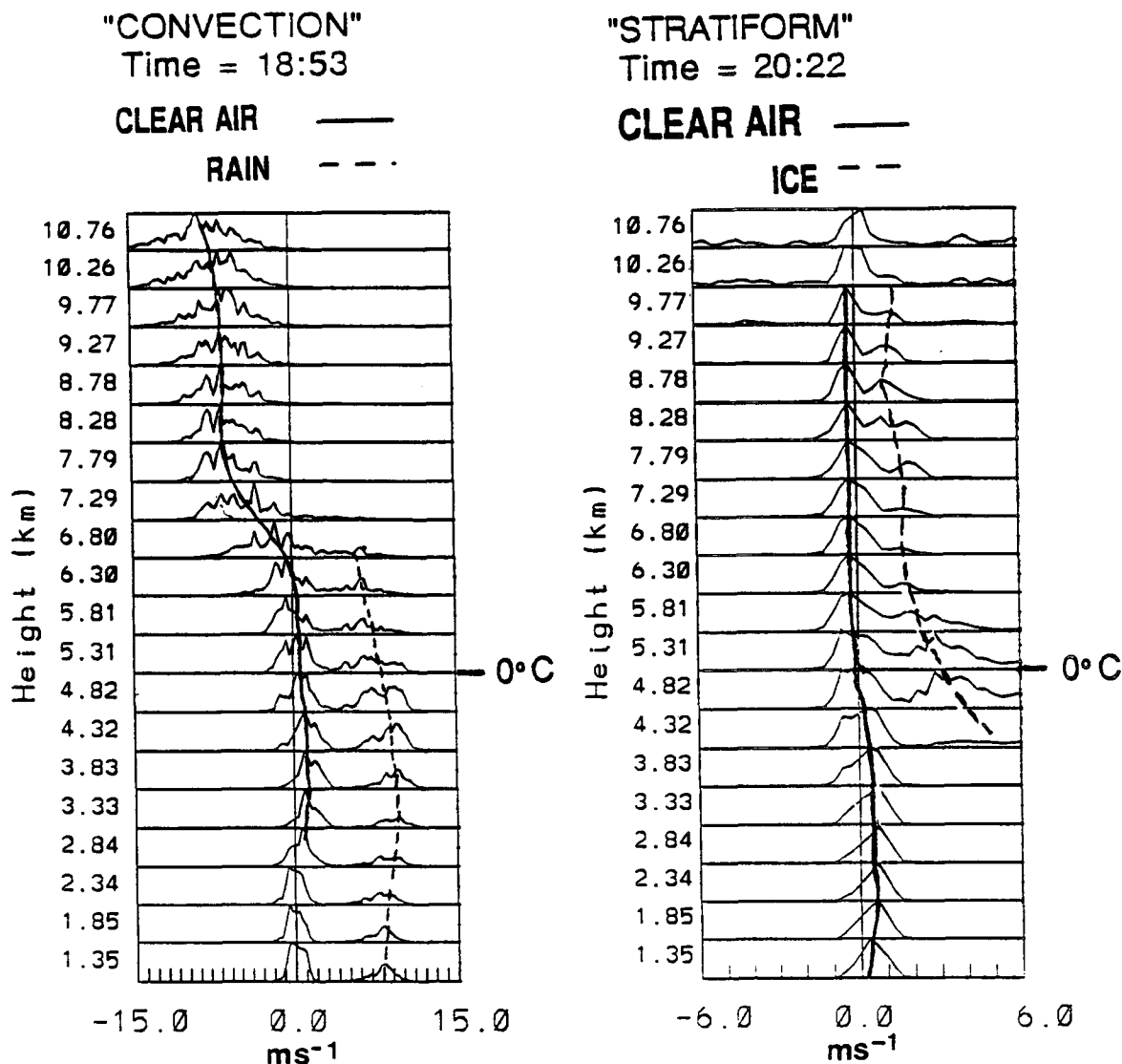## Time = 20:22

CLEAR AIR ——
ICE — —

FIG. 2. Samples of the observed radar spectra against height. (a) A section through the mature convective cell showing the edge of the convective downdraft at the lower levels and glaciation at the upper heights. The rain echo extends well above the freezing level. (b) A typical profile showing the stratiform profiles. Note the well-defined ice echoes above the freezing level and the clearly defined mesoscale up- and downdrafts. The spectra are each normalized by the maximum value, and positive is defined as toward the radar.

described, techniques have been developed for studying the pure liquid and pure ice phase size distributions using profiler data, but it remains an interesting challenge to use the fall-speed information to obtain an improved understanding of the melting layer.

The techniques described in Rajopadhyaya et al. (1993, 1994) are used to retrieve precipitating ice and raindrop size distributions from the precipitation echoes.

The reflectivity of hydrometeors is proportional to their diameter to the sixth power, and the total reflectivity is the incoherent sum over all drops within the volume. Thus the reflectivity factor Z is summed over all the hydrometeors of diameter D_i per unit volume and is expressed as (e.g., Doviak and Zrnić 1984)

$$Z = \Sigma_i D_i^6 \approx \int_0^\infty N(D) D^6 dD, \qquad (1)$$

where $N(D)$ is the number of drops in the diameter range between D and $D + dD$. Thus, the scattering is associated with the reflectivity-weighted fall-speed spectrum. This spectrum is smeared by variations in radial velocity over the beamwidth and pulse volume, but this smearing function is identical to the clear air spectral peak. Therefore, the ob-

served precipitation spectral peak may be represented by the convolution of the clear-air spectral shape and a "true" reflectivity-weighted fall-speed spectrum. Hence the observed radar spectrum $S(w)$ can be expressed as (e.g., Wakasugi et al. 1986)

$$S(w) = G(w - \bar{w}) + G(w)*P(w - \bar{w}) + n, \quad (2)$$

where $G(w)$ is a Gaussian spectrum modeling the clear air echo, P is the reflectivity-weighted fall-speed spectrum for still air, n is the noise level, $\bar{w}$ is the mean vertical wind, and "$*$" denotes a convolution. The fall speed can be converted to diameter using the fall-speed relation of Foote and du Toit (1969):

$$w(D) = [9.65 - 10.3 \exp(-600D)]\left(\frac{\rho}{\rho_0}\right)^{-0.4}, \quad (3)$$

where D is measured in millimeters, w is in meters per second, and the parameters ρ and ρ_0 are the density of the air and the density at a pressure of 1000 hPa, respectively.

Below the melting level, the estimated drop size distribution is obtained by first separating the precipitation spectrum from the clear-air spectrum at the position of minimum signal strength between them. As noted, the observed spectral peak is broader than the true reflectivity-weighted fall-speed spectrum because of the effects of beamwidth and turbulence. An estimate of the true reflectivity-weighted precipitation spectrum $P(w)$ is obtained by deconvolving the observed precipitation spectrum with the clear-air Gaussian spectrum using a Fourier transform deconvolution technique. The resulting velocity spectrum can then be converted to a diameter spectrum and a D^6 correction inserted.

The technique is fundamentally the same as that described by Gossard (1988). For details see Rajopadhyaya et al. (1993). Rajopadhyaya et al. (1993) showed that the technique obtained drop size distribution amplitudes with a precision of about 10% over a range of diameters from just under 1 mm to greater than 4 mm, which covers the bulk of the precipitating water. Comparisons of a similar analysis with aircraft data have also yielded good agreement (Rogers et al. 1993).

The estimation of ice crystal size distributions is more complicated because of the presence of many different types of ice crystals in clouds, each with their own fall-speed relations (e.g., Locatelli and Hobbs 1974). However, the retrieval process is tractable as long as a number of simplifying assumptions are made.

Retrievals of the ice size distributions are only obtained in stratiform cloud where vertical motions are weak and descending motion extends above the freezing level. This implies little supercooled water, and the small vertical velocities mean that the clear-air and ice echoes have distinct, separate peaks. This is verified by the lack of a peak in the Doppler spectrum at fall speeds greater than about 2 m s^{-1}. The lack of supercooled water implies that riming should be of little importance.

We exclude small single crystals from our consideration because the D^6 reflectivity dependence renders them essentially invisible to radar operating at this frequency. Graupel with sizes corresponding to the observed fall speeds are much smaller than the aggregates that we consider. This again implies low reflectivity per particle and unrealistically high ice contents are needed to produce the observed reflectivity.

These considerations allow us to simplify the number of ice types that need to be considered to two different types of aggregates, that is, aggregates of dendrites and aggregates of plates, bullets, and columns. This is reasonable 2–3 km above the freezing level, but we almost certainly observe large single crystals above this layer. This will introduce further errors because of the use of incorrect fall speed–size relations. Langleben's (1954) power law is used to convert the fall-velocity spectrum to its size distribution:

$$w = aD^b\left(\frac{\rho}{\rho_0}\right)^{-0.5}, \quad (4)$$

where D is the melted diameter, and a and b are functions of ice crystal density and geometry. The values of a and b used are $a = 0.8$ and $b = 0.16$ for unrimed aggregates of dendrites and $a = 0.69$ and $b = 0.41$ for aggregates of plates, columns, and bullets (hereafter referred to as plates) (Locatelli and Hobbs 1974). These fall-speed relations refer to the melted diameter, but we assume that this is proportional to the physical diameter of the particles. That is, the crystals are assumed to be of constant density.

Furthermore, we need to assume a distribution shape to solve the retrieval problem. Otherwise, there are no unique solutions with the two ice-type fall speeds. The size distributions of the ice crystals are assumed to be exponential.

A least squares fitting approach is used to fit the model spectra varying the absolute number densities and slopes of the ice size distributions. The size spectrum is converted to a reflectivity-weighted fall speed and smeared by a Gaussian function based on the observed clear-air peak as described by Eq. (2). For a detailed description of the retrieval process, its assumptions, limitations, and precision (as distinct from accuracy) see Rajopadhyaya et al. (1994). The results from simulated data suggest that the deduced size parameters have an uncertainty of 10%–20%.

To estimate the absolute size distributions, the profiler was calibrated by comparing 15-min averages of the measured precipitation echo power with weather radar reflectivity data above the profiler from the NOAA TOGA and MIT radars. Note that the sampling times and resolution volumes of the two radars were not the same. In particular, data obtained from weather radar were interpolated in height to match the profiler. With the observed scatter between the profiler precipitation echo estimates and the weather radar reflectivity

estimates, there is an uncertainty in the cross-calibration of about 0.75 dBZ. Above the freezing level a reflectivity correction for the low bulk density of the ice particles and ice dielectric constant is applied (Zrnić et al. 1993).

A number of parameters are derived from the particle-size distributions in this paper. These are the median volume diameter D_m (defined as the diameter where half of the water volume resides at diameters greater than D_m, $\int_0^{D_m} D^3 N(D) dD = \int_{D_m}^{\infty} D^3 N(D) dD$), total precipitating water volume, and a heating rate implied by the vertical gradient of the precipitation mass flux (see section 3d).

The uncertainties in the drop size distribution amplitudes due to the retrieval process have been estimated using simulations (Rajopadhyaya et al. 1993, 1994). In addition to the errors introduced by the retrieval process, there is an uncertainty in the profiler reflectivity calibration. Using a simple propagation of errors, the total relative uncertainty is estimated to be about 25% for the rain size distributions, and a similar value is therefore inferred for the total precipitating water volume. In the case of the ice retrievals we have additional uncertainties based on reflectivity corrections and the assumptions regarding ice type and density. The calibration uncertainty is again likely to be the major contributor, and a conservative estimate of the uncertainty of the amplitude of the size distribution, and hence the total precipitating mass flux, is about 40%.

For calculating the uncertainty in the heating rate, note that the calibration error is identical at the two heights that are used to calculate the gradient in water flux. The simplest way to account for this is to include the calibration error at the last stage of the heating calculation to avoid dealing with correlated errors. The resulting uncertainties will be shown in the derived rates.

With regard to the median drop diameter, the absolute error of adjacent points in the size distributions are highly correlated, and the uncertainty in the estimates is reduced to about 6%.

3. Observations of the 5 December 1989 squall line

a. Weather radar overview

The squall line formed to the south of the radar site from an initially disorganized line of cells and propagated northward at about 11 m s^{-1}. The morning sounding (not shown) modified by substituting a section close to the dry adiabat for the nocturnal inversion had a CAPE (convective available potential energy) of about 2600 J kg^{-1}, indicating substantial potential for convection. A sounding at 2030 LT through the trailing stratiform region (Fig. 3) shows a typical sounding for this location with a dry region below the freezing level (at 4.65 km). The operational sounding record did not
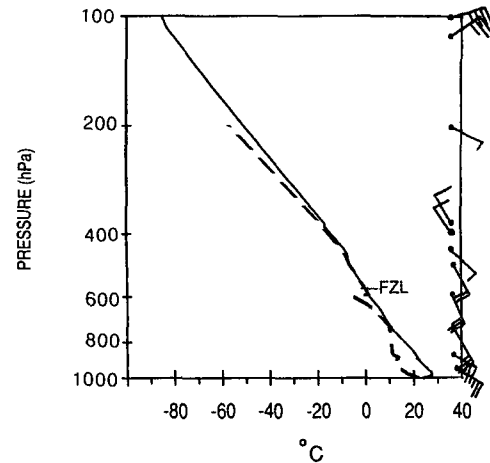

Fig. 3. Sounding at 2030 LT. The solid line is the temperature, dotted line is the dewpoint temperature, and the vectors are the horizontal winds with a barb corresponding to 5 m s^{-1} and a half-barb equal to 2.5 m s^{-1}. The 0°C point is marked as FZL.

contain the isothermal region a few hundred meters thick that was most likely present (Stewart et al. 1984). Willis and Heymsfield (1989) found this isothermal layer could be as much as 350 m thick, but may be slightly above freezing temperature. The freezing level in the 0830 soundings before and after the storm were within 100 m of the 2030 sounding shown. Recent analyses of TOGA COARE (Coupled Ocean–Atmosphere Response Experiment) data showed temperature perturbations at a given level of only 1°–2°C in active convective systems, indicating that only small changes in the freezing level were present despite the large diabatic heating (Roux 1995). Therefore, it is not expected that the freezing level moved more than a few hundred meters in height within the squall system described here. The wind measurements showed a weak rear inflow region between 900 and 600 hPa (~1– 4.5 km).

Reflectivity data from volume scans with the MIT radar have been interpolated onto a Cartesian grid. Figure 4 shows a CAPPI (constant-altitude plan position indicator scan) of the radar reflectivity at 1840 and 1940 LT for a height of 2 km along with a north–south cross section over the profiler at these times. The first shows the convective line structure that passed over the radar, while the latter period shows the trailing stratiform region.

New cells were forming at the leading edge of the cold pool (L1 near $y = 25$ km), while the line of mature cells (L2) was aligned essentially east to west at $y = 0$ km. There was an extensive region of weak reflectivity trailing the active convection. The stratiform region was growing during this period further to the south.

The north–south section clearly shows a shallow cell (C1) about 6 km deep at the leading edge of the squall. Subsequent scans (not shown) show the cell rapidly
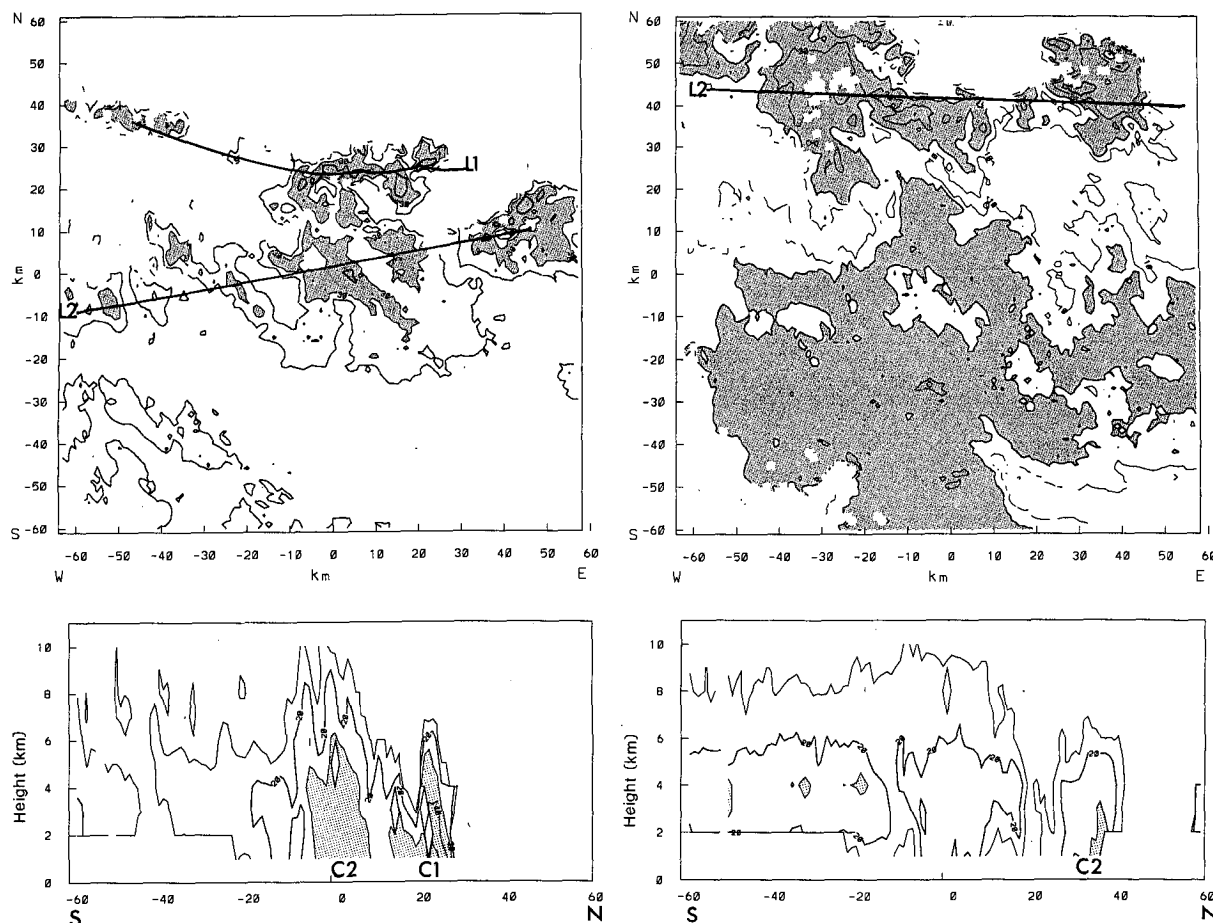
FIG. 4. Reflectivity measured by the MIT radar showing (a) a CAPPI at a height of 3 km and (b) a pseudo-RHI north–south cross section over the profiler site at 1840 LT 5 December 1989, while (c) and (d) are a CAPPI and a psuedo-RHI scans at 1940 LT. Reflectivities greater than 30 dBZ are shaded on (a), (b), and (d) to highlight regions of convection, while areas greater than 20 dBZ are shaded on (c) to delineate the stratiform rain. Contours are drawn every 10 dBZ from 20 dBZ in (a) and from 10 dBZ in (b), (c), and (d). The origin of the coordinate system marks the profiler site. The leading line of cells is marked by L1, L2 is the line of mature cells, while C1 is the leading cell passing over the profiler, and C2 is the mature cell. The north–south dashed lines in (a) and (c) mark the positions of the pseudo-RHI scans.

increased in height to well over 10 km. The leading cell is separated from a much deeper cell (C2) with similar maximum reflectivities by a region of quite low reflectivity. The mature and developing cells had similar maximum reflectivities. The reflectivity structure and evolution is typical of tropical squall lines (e.g., Houze 1977).

Figures 4c and 4d show the extensive region of low reflectivity stratiform rain. However, the RHI (range–height indicator) does exhibit some structure showing the remains of the decayed convective cells that make up this region. A bright band is clearly evident near the freezing level. The cell C2 has decreased in vertical extent and the reflectivity in the transition region behind L2 has increased by about 5 dBZ at low levels.

b. Vertical motions

The vertical motion field with 94 s resolution up to 11 km observed by the profiler is shown in Fig. 5. The

field shows the basic structure discussed in the conceptual model of Houze (1989). There was a highly convective region with large vertical motions, a well-defined transition region with deep descent, and a stratiform region with a mesoscale up- and downdraft couplet with the change from ascent to descent at about 1 km above the freezing level (4.65 km).

The vertical motions in the convective region show the two main convective cells separated by a narrow region of deep descending motion. The first was a relatively shallow intense cell (C1, 1807–1823) with a local maximum in upward velocities below 3 km of about 6 m s^{-1}, coinciding with the upper limit in height of the 40 dBZ reflectivity contour in Fig. 4a. There is a second upward velocity maximum in this cell at and above the freezing level. The acceleration, together with the observation that the intense updraft does not extend far above the freezing level, indicates that glaciation and its concomitant drop-unloading of the pre-
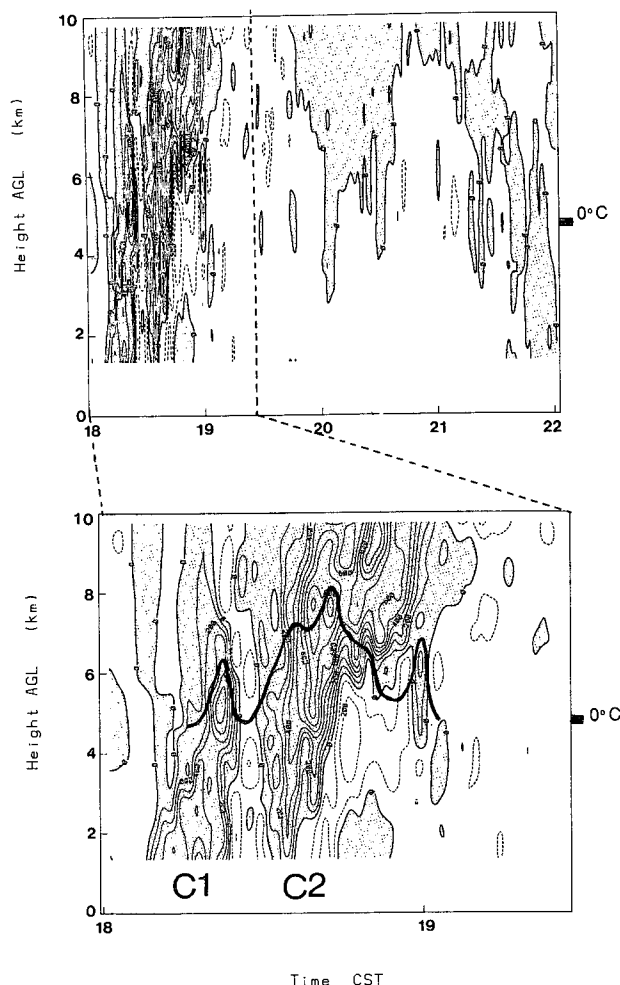
FIG. 5. Time–height cross sections of the vertical motion detected by the profiler showing the convective region (lower frame) and the storm as a whole (upper frame). Contours are drawn every 1 m s^{-1} and upward motion is shaded. The heavy line in the lower panel denotes the maximum height at which rain echoes were visible. Cells C1 and C2 are as in Fig. 4. The labels along the bottom mark the convective (C), transition (T), and stratiform (S) precipitation over the profiler.

cipitation was only just beginning. This was consistent with the cell top rapidly increasing in height as ice processes become important. There is significant upward vertical motion extending well above the weather radar reflectivity top, probably reflecting the cloud top being greater than the maximum height of significant radar reflectivity. As just noted, the reflectivity profile of this cell was only about 6 km deep at this time. The low-level velocity and reflectivity maximum along with the rapid intensification from reflectivities less than 20 dBZ 10 min prior to the passage over the profiler are likely indications of warm rain processes and condensational heating in the early stage of the cell's development.

The region of descending motion separating the two cells matched the region of low reflectivity between the two cells discussed in the previous section.

The mature cell (C2, 1830–1853) reached to great heights and a pronounced acceleration above the freezing level was observed, with velocities in excess of 10 m s^{-1}. However, in the lowest 2 km there were significant descending motions. Evaporation and drop loading were clearly important and the cell was most likely developing a pronounced cold pool. This was consistent with the new cell developing ahead of the mature cell, in the region of convergence between the cold pool outflow and the environmental flow. These factors also indicate that the mature cell was effectively in decline as the source of low-level high-equivalent-potential-temperature air has been closed off (Houze 1977). The decline is confirmed by the maximum reflectivity within the deep cell observed with the Doppler radar decreasing after it had passed the profiler site (Fig. 4d).

A lower limit to the draft-core diameters can also be inferred from the profiler data. A single 94-s sample corresponds to an average over a distance of approximately 850 m at the cell propagation speed (estimated from successive C-band radar scans). LeMone and Zipser (1980) defined a vertical motion core as a vertical velocity greater than 1 m s^{-1} over a horizontal distance of greater than 500 m. Data for three heights are shown in Fig. 6 along with a length scale. Several features are apparent. In cell C1, the low-level diameter of the updraft core is over 6 km, decreasing to 2.8 near the freezing level and not extending far above that height. In the mature cell C2, the opposite structure is seen, barely satisfying the core criterion at 1.85 km, over a 5-km diameter near the freezing level and greater than 13 km at a height of 7.8 km. The downdraft cores tend to be smaller and are much less intense. This sample is too small for a statistical study, but it is clear that the core diameters tend to be larger than in GATE [GARP (Global Atmospheric Research Program) Atlantic Tropical Experiment] data (LeMone and Zipser 1980; Zipser and LeMone 1980), and there is no evidence of the downdraft cores having larger diameters than the more intense updrafts, as was seen in the GATE data.

As noted, the acceleration at the level of freezing in the convective region was consistent with glaciation and drop-unloading. Another factor that may be important is associated with the thermodynamic profile. It is at about 7 km that the sounding and moist adiabat used in a CAPE calculation rapidly diverge so that more convective energy is available for the upward motion.

The transition region between the active convective line and the stratiform region was well defined. It had deep descending motion throughout the column. This acts to partially balance the deep upward motions in the convective regions. The transition region was much wider in time and spatial extent here than in a number

1354 (m)   1848 (m)

2342 (m)   2836 (m)

Log N(D)

3330 (m)   3824 (m)

Diameter (mm)

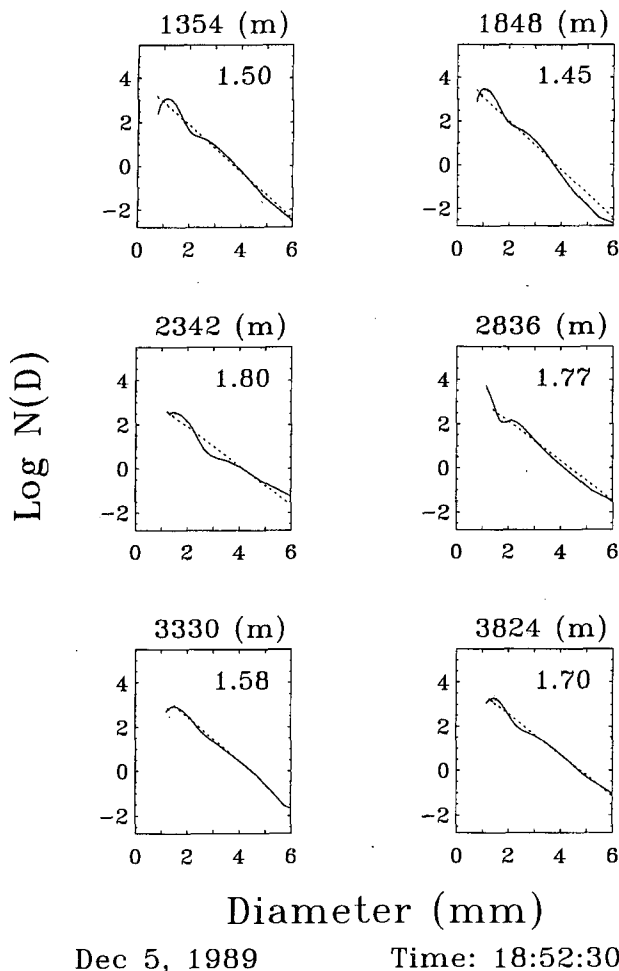Dec 5, 1989   Time: 18:52:30

FIG. 6. Time series of the vertical motions observed with the profiler. Each estimate is an average over 94 s. Successive heights are offset by 10 m s^{-1}, and the dashed lines represent ±1 m s^{-1} to show the draft cores. Velocities with magnitudes greater than 1 m s^{-1} are shaded. A length scale is shown in the top left as a reference to the approximate time corresponding to a length scale of 5 km. Cells C1 and C2 are as in Fig. 5.

of similar systems that we have observed with the Darwin profiler, but as the system passed over the profiler there was a general increase in reflectivity level, possibly associated with the decay of C2. A possible scenario is that the increase in reflectivity arises from ice particles detrained from C2 and accelerated downward by the deep descent in the transition region.

The stratiform region showed a typical mesoscale up- and downdraft structure with vertical velocities of about 10–30 cm s^{-1}, comparable to the observations of Zipser (1977). Note that the crossover from down to upward velocities occurs above the melting level and tends to slope upward away from the convective part of the storm except adjacent to the transition region. There were wavelike variations in the crossover height between upward and downward motion, but this is not reflected in the vertical velocity field at heights away from the crossover. The slope was consistent with descending rear inflow, as was seen extending to the active convective region in the Doppler weather radar data (not shown). The magnitudes of the vertical motions were quite uniform. The mean vertical motion averaged over the stratiform region (1937–2050) showed descent below 7.5 km because the downdrafts were stronger than the updrafts. After 2050 the vertical motion became downward over all heights as the storm decayed, with further rain gradually decreasing.

c. Precipitation characteristics

Rain echoes were clearly observed for more than 3 h. The period covered the latter part of the mature convective cell, the transition and stratiform region. As mentioned earlier, distinct ice echoes were also observed throughout much of the period during which the stratiform region was over the profiler.

The regions of very strong upward motion lift considerable amounts of supercooled water. Figure 2 shows that the rain spectral peak at fall speeds of about 8 m s^{-1} extended above the freezing level. The maximum height at which the liquid water echo was observed is shown by the heavy line in Fig. 5 overlaying the convective vertical motions. The strongest updrafts took supercooled rainwater to heights of up to 8 km. The maximum acceleration occurred at the same heights at which the supercooled water froze, releasing latent heat and decreasing the drag associated with falling drops.

Figure 7 shows a sample of the 15-min-averaged size distributions at different heights during the latter convective period. The lower solid line is the estimated size distributions, and the dotted line is a least squares fit using an exponential size distribution. The figure clearly shows a bulge in the distributions near a diameter of 3 mm and evidence of a peak near 1 mm. However, the overall shape of the distributions are reasonably well approximated by an exponential distribution. The distributions in the transition and stratiform regions are very close to exponential. Similar findings have also been reported by aircraft directly sampling drop size distributions during TOGA COARE (Willis et al. 1995). The radar spectra indicated a distinct separate peak at diameters of less than about 0.5 mm, but the peaks were very close to the clear-air peak and no quantitative retrievals were possible.

Because the raindrop distributions were reasonably approximated by an exponential function, the distributions were categorized by the total precipitating liquid water and the median volume diameter D_m.

The ice retrieval parameterizes the distributions by the median volume diameter of aggregates of plates and aggregates of dendrites. The median sizes and number densities of the two types of aggregates were reasonably similar and have been combined to give a single median volume diameter.
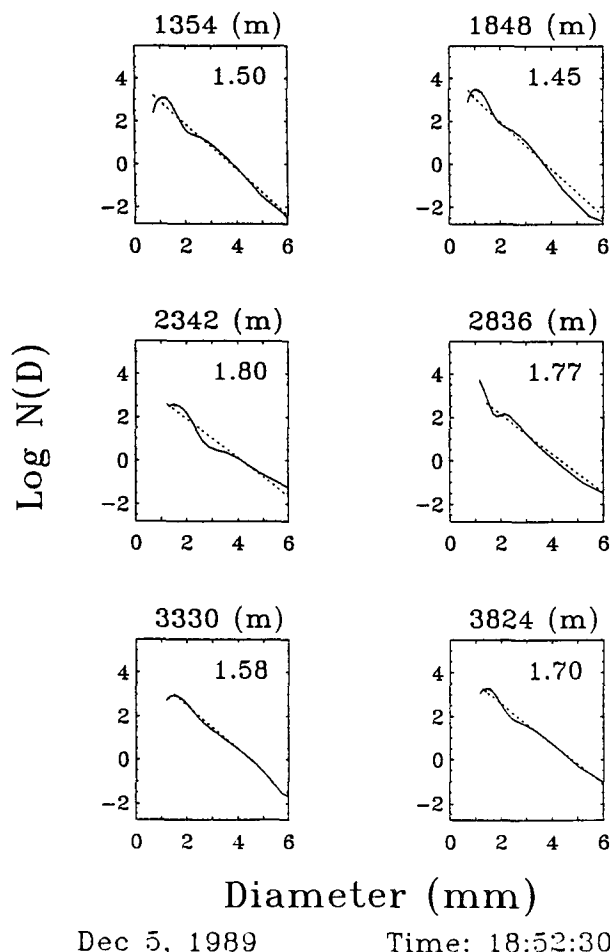
FIG. 7. Fifteen-minute averages of the observed raindrop size distributions. The units are mm for the x axis and $\log_{10}$(number of drops per cubic meter) for the y axis.
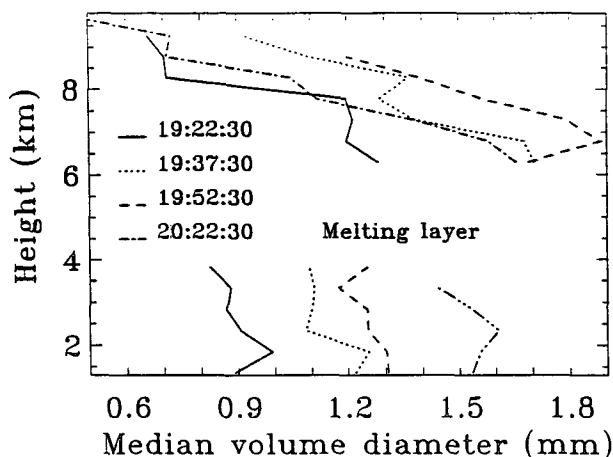

FIG. 8. Profiles of 15-min averages of the median volume diameter of the precipitation between 1915 and 2030. It was not possible to retrieve ice size distributions after this time.

iform region were gradual. The maximum in ice size occurred before the raindrop size maximum.

The size distributions have been integrated to obtain the total precipitating water content for drops larger than 1 mm in diameter (Fig. 10). In both the transition and stratiform regions the water content showed a similar vertical structure, with a maximum inferred near the melting level. However, the increase in total water was less than indicated by the median volume diameter, showing that accretion of the aggregates was ongoing and important. This also suggests that condensation in the mesoscale updraft was of lesser importance, a conclusion similar to Gamache and Houze (1983) based on composite radar and aircraft studies. However, the total liquid water and temperature are in the regime where both condensation and aggregation of the particles were important (Williams et al. 1994). Conden-
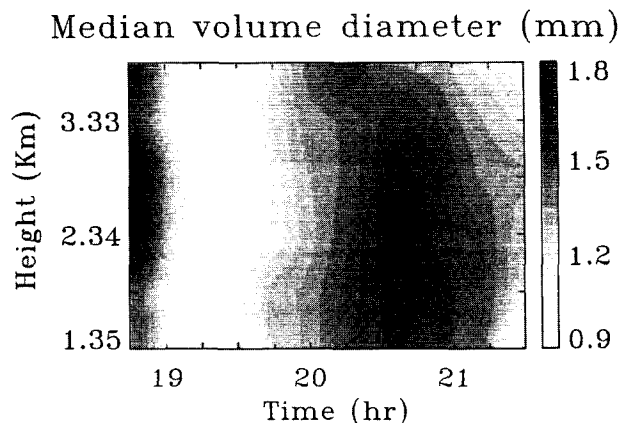
Profiles of the median diameter are shown in Fig. 8. Above the melting layer the ice particles grew as they fell, with the median volume diameter doubling between 9.5 and 6.5 km. Significant rain echoes were visible long after it was possible to retrieve ice characteristics. Also, the median diameters below the melting level decreased by about 30%. This is further evidence of significant drop breakup when the ice aggregates melt. There was a slight tendency for droplet regrowth as they fell.

Because rain retrievals were possible over a longer period than the ice retrievals, a time–height cross section over the entire time that rain echoes were useable is shown (Fig. 9). The transition region, as expected by its small radar reflectivity, had the smallest drops and ice aggregates. The convective region had large changes in time and height. Also, it was not possible to retrieve the size information in the areas of strongest convection because of the large variations in vertical velocity. The temporal variation of the sizes in the strat-

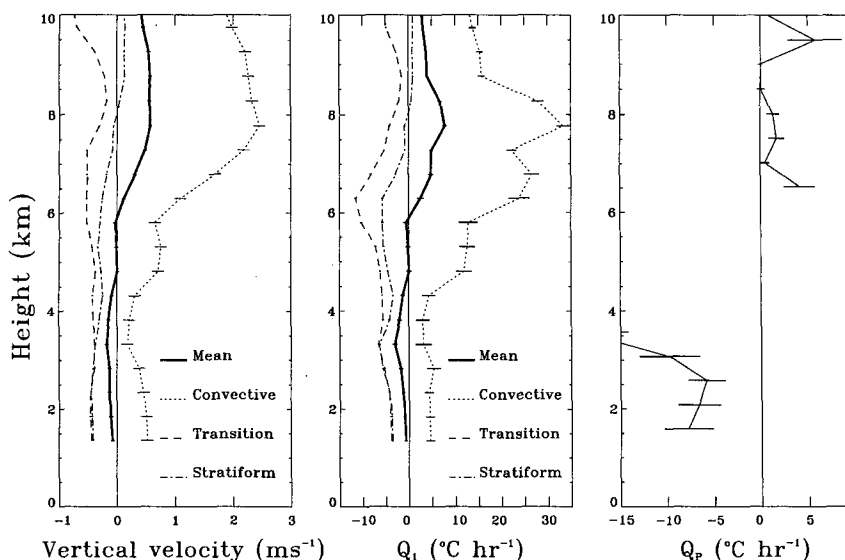FIG. 9. Time–height cross section of the median volume diameter (mm) between 1845 and 2130.

FIG. 10. Time–height cross section of total precipitating water (g m^{-3}). Labels C, T, and S are as in Fig. 5. There are no data below the dashed line at a height of 1.35 km.

sation was probably more important for the larger particles (Williams et al. 1991).

There is a distinct maximum in water content at the edge of the convective region followed by a minimum in the transition region. The structure in the stratiform region is more complex with a maximum below the freezing level near 1940 LT, composed mainly of small drops (Fig. 9). The maximum above the melting level occurs somewhat later and appears to be feeding the secondary maximum at the lower levels after about 2000 LT. No ice echoes were detectable after the cessation of the mesoscale updraft and the water content at the lower levels after this decreased steadily. This marked the decay phase of the system.

Below the melting level, as expected, there was considerable evaporation, with over half of the volume evaporating between 4- and 2-km altitudes. Although there was less water in the transition region, the rate of evaporation was similar to that in the stratiform region.

d. Heating rates

The profiles of vertical motion and precipitation size distributions allow us to estimate heating profiles.

The sensible heating rate Q_1 is related to the vertical motion and static energy ($s = gz + c_pT$) profiles. Following Frank and McBride (1989) and neglecting a storage term that is small, we can write:

$$Q_1 \approx \left(\overline{\nabla \cdot s\mathbf{V}} + \frac{\partial \overline{\omega s}}{\partial p} \right), \tag{5}$$

where ω is the vertical motion in pressure (p) coordinates, $\mathbf{V}$ is the horizontal wind vector, and ∇ is the horizontal divergence operator. The horizontal gradi-

ents of s are usually small and the term $s\nabla\mathbf{V}$ is approximately $-s\partial\omega/\partial p$ by continuity. Therefore,

$$Q_1 \approx \overline{\omega} \frac{\partial \overline{s}}{\partial p}, \tag{6}$$

although the term $\mathbf{V}\nabla \cdot s$ may be significant in the convective region where there are very large heating rates. Our estimate of s is based on a sounding at 2030 LT. This analysis uses a direct measure of the vertical motion and does not assume mass balance or boundary conditions as in radiosonde-based calculations of Q_1 (Yanai et al. 1973; Frank and McBride 1989).

A heating rate associated with the precipitation can also be calculated. The vertical mass flux of precipitation is given by $(\pi/6) \int_0^\infty wN(D)D^3 dD$, so the heating associated with the precipitation is simply

$$Q_P = \frac{L\rho\pi}{6} \frac{\partial}{\partial z} \left[\int_0^\infty wN(D)D^3 dD \right], \tag{7}$$

where L is the latent heat of vaporization for estimates below the freezing level and for sublimation above the freezing level, ρ is the density of water, and w is the fall speed of a particle of diameter D as defined previously. Above the freezing level this will be an upper bound of the Q_P, because it implicitly assumes that condensation of vapor onto the ice is the dominant growth process, whereas our previous observations suggest aggregation is the more important process.

Figure 11 shows profiles of the mean vertical motion, Q_1 and Q_P, for the period from 1800 to 2145 LT covering the time that the storm system was over the profiler. The magnitude of the heating rates was an order of magnitude greater than those given by Frank and
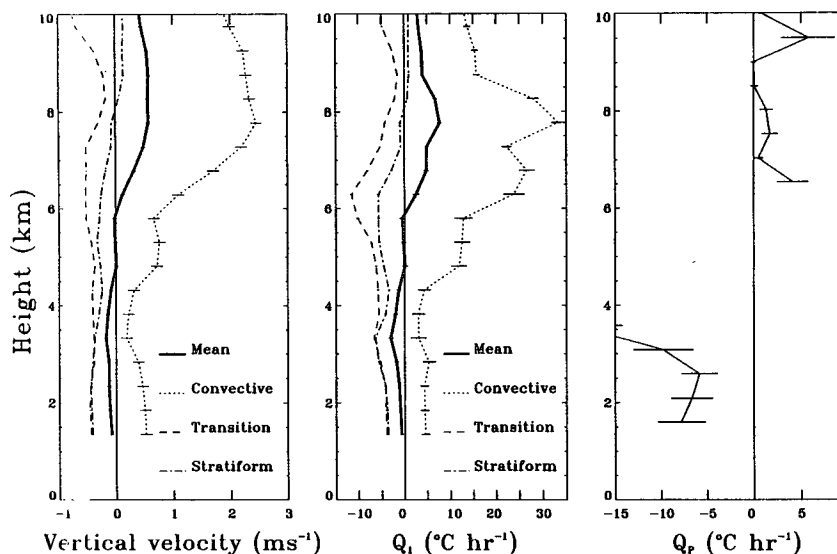
FIG. 11. Profiles of the overall mean (heavy solid line), convective (dotted line, 1800–1905), transition (dashed line, 1907–1935), and stratiform (dot–dashed line, 1937–2047) vertical motion field, Q_1 profiles, and Q_p profiles; Q_p is calculated from 1915 to 2030.

McBride (1989), but their calculations were over the AMEX (Australian Monsoon Experiment) domain of about 2×10^5 km^2, compared to the squall dimensions of about 1.5×10^4 km^2. Therefore, the amplitude of the rates is consistent with the Frank and McBride analyses at the upper levels. The results for the convective and stratiform regions separately are also consistent with the profiles from a number of experiments shown by Houze (1989). However, the descending motion below 4.5 km over the total observing period gives a cooling rather than a heating, a finding at variance with the large-scale findings of these other studies.
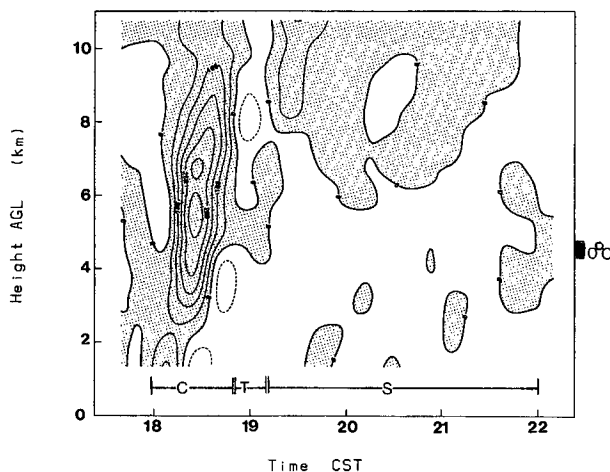

FIG. 12. Time–height cross section of 15-min averages of the vertical motion observed between 1730 and 2200 12 January 1990. Labels C, T, and S are as in Fig. 5.

The profile of Q_p closely matched the Q_1 profile for the transition and stratiform regions. This is quantitative evidence that the mesoscale circulation in the stratiform region is directly driven by ice crystal growth above the melting level and evaporation below. The descent above the melting level in the transition region was driven by other processes.

4. Comparison with the 12 January 1990 monsoon squall

There was another well-sampled storm on 12 January 1990 that has been analyzed. This particular case is the same one as analyzed by Keenan and Rutledge (1993). This storm formed north of Darwin during an active monsoon phase. It was thus an oceanic storm rather than a continental storm as has just been discussed.

This case showed many similarities in the vertical motion field (Fig. 12). Again a mature, highly glaciated cell was sampled with a dramatic upward acceleration near the freezing level and a convective downdraft undercutting the cell as the cold pool advanced ahead of the storm. The transition region in this storm was much narrower, but again there was descending motion throughout the troposphere and a trailing stratiform region with a mesoscale up- and downdraft couplet. The trailing stratiform region was more extensive in this case and was largely made up of decayed convective cells (Keenan and Rutledge 1993). There was also more structure in the stratiform vertical motion field than in the 5 December case, possibly associated with some remnants of the old convective cells.

The precipitation characteristics were also very similar to the previous case. There were similar variations in median size and total precipitation against height as in the 5 December case showing the growth of the aggregates as they fall and the growth of the large drops as they fall in the stratiform region. The increase in D_m was probably related to the depletion of small drops by relatively large evaporation rates of the small drops. Again the transition region had similar evaporation rates as the stratiform region, but with even less total water.

The mean vertical motion over the whole storm period and its phases are shown in Fig. 13, and again, the result is similar to the 5 December case. In particular there was mean descending motion below 3 km.

A remarkable feature of these two storms is just how similar the draft and precipitation structure appear. A number of other storms that were not as well sampled have also been analyzed, and again there is general consistency in their structure. The mean decent at the lower levels may be related to the stage of the life cycle that was observed, with the presence of mature convective cells with well-developed convective downdrafts and the extensive transition and stratiform region with its mesoscale descent. It is possible that different results would be obtained if a younger system were sampled. Frank and McBride (1989) did, however, observe mean ascent at all stages of storm evolution.

5. Conclusions

The observed vertical motion and precipitation characteristics of a well-developed tropical squall line have been discussed in detail. The vertical motion field generally fits well with the conceptual model of Houze (1989) and others. This includes the mean acceleration above the freezing level in the convective part of the storm, the deep descent in the transition region, and the mesoscale up- and downdraft couplet in the stratiform region. The amplitudes of the updrafts were similar to those reported in GATE by LeMone and Zipser (1980), but with a more pronounced acceleration above the freezing level. The downdrafts at the upper levels were much weaker than those of LeMone and Zipser (1980). The diameters of the convective cores. were larger than those observed during GATE (LeMone and Zipser 1980; Zipser and LeMone 1980).

In particular the effect of glaciation and drop-unloading have been explicitly observed in the mature convective cell. The observations suggest that warm rain processes generate significant rain in the newly developing cells without ice physics. The importance of the convective downdraft in the overall circulation has also been observed. Heating rates diagnosed from the mean vertical motion show a net cooling in the lower levels in contrast to the results based on radiosonde networks (e.g., Frank and McBride 1989) and other studies (e.g., Houze 1989), although this latter
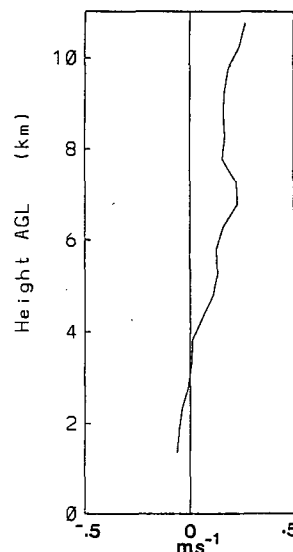

FIG. 13. Mean vertical motion for the 12 January 1990 squall line.

paper did present a mean heating profile with small values below 4 km, suggesting a balance between convective ascent and stratiform descent. Our mean low-level cooling may also be in part a function of the sampling of a squall in its mature to decaying stage.

The precipitating particle distribution tends to show a growth in median volume diameter as the precipitation falls. Above the melting level this growth is seen as increased total water volume at lower heights, but once below the melting layer, evaporation becomes very important. About half of the water volume is lost to evaporation below the melting level. The growth of ice aggregates above the melting level and evaporation below drive the observed circulation stratiform region and the descent below the melting level in the transition region. The upper-level descent is probably a dynamical response to the large vertical motions above the freezing level in the convective cells. The profiles of total volume are quite consistent with the cloud modeling study of a midlatitude squall system by Rutledge and Houze (1987).

REFERENCES

Augustine, J. A., and E. J. Zipser, 1987: The use of wind profilers in a mesoscale experiment. *Bull. Amer. Meteor. Soc.,* **68,** 4–17.

Balsley, B. B., W. L. Ecklund, D. A. Carter, A. C. Riddle, and K. S. Gage, 1988: Average vertical motions in the tropical atmosphere observed by a radar wind profiler on Pohnpei (7N latitude, 157E longitude). *J. Atmos. Sci.,* **45,** 396–405.

Chilson, P. B., C. W. Ulbrich, M. F. Larsen, P. Perillat, and J. E. Keener, 1993: Observations of a tropical thunderstorm using a vertically pointing, dual-frequency collinear beam Doppler radar. *J. Atmos. Oceanic Technol.*, **10**, 663–673.

Cifelli, R., and S. A. Rutledge, 1994: Vertical motion structure in maritime continent mesoscale convective systems: Results from a 50-MHz profiler. *J. Atmos. Sci.*, **51**, 2631–2652.

Doviak, R. J., and D. S. Zrnić, 1984: *Doppler Radar and Weather Observations.* Academic Press, 458 pp.

Foote, G. B., and P. S. du Toit, 1969: Terminal velocity of raindrops aloft. *J. Appl. Meteor.*, **8**, 249–253.

Frank, W. M., and J. L. McBride, 1989: The vertical distribution of heating in AMEX and GATE cloud clusters. *J. Atmos. Sci.*, **46**, 3464–3478.

Fukao, S., K. Wakasugi, T. Sato, S. Morimoto, T. Tsuda, I. Hirota, I. Kimura, and S. Kato, 1985: Direct measurement of air and precipitation particle motion by very high frequency Doppler radar. *Nature*, **316**, 712–714.

Gamache, J. F., and R. A. Houze Jr., 1983: Water budget of a mesoscale convective system in the Tropics. *J. Atmos. Sci.*, **41**, 1835–1850.

Gossard, E. E., 1988: Measuring drop-size distributions in clouds with a clear air sensing Doppler radar. *J. Atmos. Oceanic Technol.*, **5**, 640–649.

Houze, R. A., Jr., 1977: Structure and dynamics of a tropical squall line system. *Mon. Wea. Rev.*, **105**, 1540–1567.

——, 1989: Observed structure of mesoscale convective systems and implications for large scale heating. *Quart. J. Roy. Meteor. Soc.*, **115**, 425–461.

Keenan, T. D., and R. E. Carbone, 1992: A preliminary morphology of precipitation systems in tropical northern Australia. *Quart. J. Roy. Meteor. Soc.*, **118**, 283–326.

——, and S. A. Rutledge, 1993: Mesoscale characteristics of monsoonal convection and associated stratiform precipitation. *Mon. Wea. Rev.*, **121**, 352–374.

Langleben, M. P., 1954: The terminal velocity of snowflakes. *Quart. J. Roy. Meteor. Soc.*, **80**, 174–181.

Larsen, M. F., and J. Rottger, 1987: Observations of thunderstorm reflectivities and Doppler velocities measured an VHF and UHF. *J. Atmos. Oceanic Technol.*, **4**, 151–159.

LeMone, M. A., and E. J. Zipser, 1980: Cumulonimbus vertical velocity events in GATE. Part I: Diameter, intensity and mass flux. *J. Atmos. Sci.*, **37**, 2444–2457.

Locatelli, J. D., and P. V. Hobbs, 1974: Fall speeds and masses of solid precipitation particles. *J. Geophys. Res.*, **79**, 2185–2197.

Mapes, B., and R. A. Houze Jr., 1993: An integrated view of the 1987 Australian monsoon and its mesoscale convective systems. Part 2: Vertical structure. *Quart. J. Roy. Meteor. Soc.*, **119**, 733–754.

May, P. T., 1991: Recent developments and performance of radar wind profilers and RASS. *Aust. Meteor. Mag.*, **39**, 237–245.

——, T. Sato, M. Yamamoto, S. Kato, T. Tsuda, and S. Fukao, 1989: Errors in the determination of wind speed with Doppler radars. *J. Atmos. Oceanic Technol.*, **6**, 235–242.

Rajopadhyaya, D. K., P. T. May, and R. A. Vincent, 1993: A general approach to the retrieval of raindrop size distributions from wind profiler Doppler spectra: Modeling results. *J. Atmos. Oceanic Technol.*, **10**, 710–717.

——, ——, and ——, 1994: The retrieval of ice particle size information from VHF wind profiler Doppler spectra. *J. Atmos. Oceanic Technol.*, **11**, 1559–1568.

Ralph, F. M., M. Crochet, and S. V. Venkateswaran, 1993: Observations of a mesoscale ducted gravity wave. *J. Atmos. Sci.*, **50**, 3277–3291.

Rasmussen, E. N., and S. A. Rutledge, 1993: Evolution of quasi-two-dimensional squall lines. Part I: Kinematic and reflectivity structures. *J. Atmos. Sci.*, **50**, 2584–2606.

Rogers, R. R., D. Baumgardner, S. A. Ether, D. A. Carter, and W. L. Ecklund, 1993: Comparison of raindrop size distributions measured by a radar wind profiler and by airplane. *J. Appl. Meteor.*, **32**, 694–699.

Roux, F., 1995: Thermodynamic structure and evolution of mesoscale convective systems observed with airborne Doppler radar during TOGA-COARE. Preprints, *21st Conf. on Hurricanes and Tropical Meteorology*, Miami, FL, Amer. Meteor. Soc., 434–436.

Rutledge, S. A., and R. A. Houze Jr., 1987: A diagnostic modelling study of the trailing stratiform region of a mid-latitude squall line. *J. Atmos. Sci.*, **44**, 2640–2656.

——, E. R. Williams, and T. D. Keenan, 1992: The Down Under Doppler and Electricity Experiment (DUNDEE): Overview and preliminary results. *Bull. Amer. Meteor. Soc.*, **73**, 3–16.

Stewart, R. E., J. D. Marwitz, J. C. Pace, and R. E. Carbone, 1984: Characteristics through the melting layer of stratiform clouds. *J. Atmos. Sci.*, **41**, 3227–3237.

Wakasugi, K., A. Mizutani, M. Matsuo, S. Fukao, and S. Kato, 1986: A direct method for deriving drop-size distribution and vertical air velocities from VHF Doppler radar spectra. *J. Atmos. Oceanic Technol.*, **3**, 623–629.

Williams, E., R. Zhang, and J. Rydock, 1991: Mixed phase microphysics and cloud electrification. *J. Atmos. Sci.*, **48**, 2195–2203.

——, ——, and D. Boccippio, 1994: Microphysical growth state of ice particles and large scale electrical structure of clouds. *J. Geophys. Res.*, **99**, 10 787–10 792.

Willis, P. T., and A. J. Heymsfield, 1989: Structure of the melting layer in mesoscale convective system stratiform precipitation. *J. Atmos. Sci.*, **46**, 2008–2025.

——, R. A. Black, F. D. Marks, and D. Baumgardner, 1995: Airborne rain drop size distributions in TOGA COARE. Preprints, *21st Conf. on Hurricanes and Tropical Meteorology*, Miami, FL, Amer. Meteor. Soc., 431–433.

Yanai, M. S., S. Esbenson, and J. H. Chu, 1973: Determination of bulk properties of tropical cloud clusters from large scale heat and moisture budgets. *J. Atmos. Sci.*, **30**, 611–627.

Zipser, E. J., 1977: Mesoscale and convective scale downdrafts as distinct components of squall line structure. *Mon. Wea. Rev.*, **105**, 1568–1589.

——, and M. A. LeMone, 1980: Cumulonimbus vertical velocity events in GATE. Part II: Synthesis and model core structure. *J. Atmos. Sci.*, **37**, 2458–2469.

Zrnic, D. S., N. Balakrishnan, C. L. Ziegler, V. N. Bringi, K. Aydin, and T. Matejka, 1993: Polarimetric signatures in the stratiform region of a mesoscale convective system. *J. Appl. Meteor.*, **32**, 678–693.